

Air pollutant concentration fluctuations in an industrial site: A wind tunnel study

*Original*

Air pollutant concentration fluctuations in an industrial site: A wind tunnel study / Schiavini, Claudia; Marro, Massimo; Ravina, Marco; Panepinto, Deborah; Zanetti, Mariachiara; Soulhac, Lionel; Salizzoni, Pietro. - In: JOURNAL OF WIND ENGINEERING AND INDUSTRIAL AERODYNAMICS. - ISSN 0167-6105. - 270:(2026). [10.1016/j.jweia.2026.106339]

*Availability:*

This version is available at: 11583/3008317 since: 2026-03-06T10:11:08Z

*Publisher:*

Elsevier

*Published*

DOI:10.1016/j.jweia.2026.106339

*Terms of use:*

This article is made available under terms and conditions as specified in the corresponding bibliographic description in the repository

*Publisher copyright*

(Article begins on next page)



Contents lists available at ScienceDirect

## Journal of Wind Engineering &amp; Industrial Aerodynamics

journal homepage: [www.elsevier.com/locate/jweia](http://www.elsevier.com/locate/jweia)

## Air pollutant concentration fluctuations in an industrial site: A wind tunnel study

Claudia Schiavini <sup>a,b</sup>,\* , Massimo Marro <sup>b</sup>, Marco Ravina <sup>a</sup>, Deborah Panepinto <sup>a</sup>,  
 Mariachiara Zanetti <sup>a</sup>, Lionel Souhac <sup>b</sup>, Pietro Salizzoni <sup>a,b</sup>

<sup>a</sup> Department of Environment, Land and Infrastructure Engineering (DIATI), Politecnico di Torino, corso Duca degli Abruzzi 24, 10129 Torino, Italy

<sup>b</sup> Ecole Centrale de Lyon, CNRS, Universite Claude Bernard Lyon 1, INSA Lyon, LMFA, UMR5509, 69130 Ecully, France

## ARTICLE INFO

## Keywords:

Pollutant dispersion  
 Concentration fluctuations  
 Scalar distribution  
 Toxicity risk  
 Wind tunnel  
 Complex industrial site

## ABSTRACT

The accidental release of hazardous airborne pollutants on industrial sites creates risks associated with the exceedance of toxicity or explosivity limits. Capturing these risks requires predicting higher-order statistics of concentration fluctuations at various distances from the source. This challenge, already complex in atmospheric boundary layers, is further complicated by the typical built environment of industrial sites. To address this, we conducted wind-tunnel experiments on the dispersion of a passive scalar from a localized ground-level source within a reduced-scale model of an industrial site. The experiments measured the velocity and concentration fields, while varying the geometry of an upstream building simulating typical complex industrial structures.

A key focus of our investigation is the one-point passive scalar concentration PDF, whose experimental realizations were systematically compared to three analytical models: the gamma, two-parameter Weibull and lognormal distributions. The gamma distribution generally provides the best predictions, although the lognormal model performs better within the building wake near the source. While the main discrepancies between theoretical distributions and experimental data consistently occur at low concentration values, all three distributions accurately predict the 95th and 99th concentration percentiles. Thus, peak and hazardous concentration levels can be reliably estimated even without fully capturing the complete concentration distribution.

## 1. Introduction

Accidental events at industrial sites, such as fires and chemical leaks, frequently lead to the release of hazardous airborne pollutants. Once emitted, these pollutants are dispersed by atmospheric turbulence, forming highly fluctuating plumes. At a fixed location downwind of the source, the concentration exhibits strong variability across a wide range of time scales, with intermittent peaks reaching up to 50 times the mean value (Lim and Vanderwel, 2023). Such extreme fluctuations can cause local concentrations to exceed critical thresholds for toxicity or flammability, even when the time-averaged mean remains safely below those limits. As a result, relying solely on mean concentration values is inadequate for assessing the true risk of hazardous exposure. Accurate modeling of concentration fluctuations, across both temporal and spatial scales, is therefore essential for effective risk assessment and mitigation.

To address this problem, numerous field and laboratory experiments have been conducted, primarily focusing on pollutant releases from localized sources, such as point and line releases, in boundary layer flows

over flat terrain, as reviewed by Cassiani et al. (2020). To model the one-point concentration PDF observed experimentally, several analytical relations were tested. Most of them are two-parameter distributions, having the advantage that the whole PDF can be obtained from only the mean  $\bar{C}$  and the variance  $\sigma_C^2$  of the pollutant concentration (Hanna, 1984). As discussed by Cassiani et al. (2020), among all models, mainly the gamma, lognormal and Weibull distributions reproduced most accurately the experimental results. However, determining which statistical distribution describes better the concentration probability density function (PDF) is not evident, and depends on experimental conditions, notably the Reynolds and Schmidt numbers, the source site position and geometry (point, line, area).

The case of a steady release from a point source over flat terrain was investigated in the seminal wind tunnel experiments of Fackrell and Robins (1982a,b). These experiments provided a detailed characterization of the influence of source characteristics on concentration fluctuations and have since served as a reference case for validating

\* Corresponding author. Department of Environment, Land and Infrastructure Engineering (DIATI), Politecnico di Torino, corso Duca degli Abruzzi 24, 10129 Torino, Italy.

E-mail address: [claudia.schiavini@polito.it](mailto:claudia.schiavini@polito.it) (C. Schiavini).

<https://doi.org/10.1016/j.jweia.2026.106339>

Received 16 June 2025; Received in revised form 18 December 2025; Accepted 8 January 2026

Available online 10 January 2026

0167-6105/© 2026 The Authors. Published by Elsevier Ltd. This is an open access article under the CC BY-NC-ND license (<http://creativecommons.org/licenses/by-nc-nd/4.0/>).

numerical models (Xie et al., 2007; Cassiani et al., 2024). In particular, they examined the impact of source height and diameter, with a focus on two key metrics: the intermittency of the single-point concentration signal (probability of non-zero concentrations) and the intensity of the concentration fluctuations  $i_c = \sigma_c/\bar{C}$ . A decade ago, Nironi et al. (2015) replicated the wind tunnel study of Fackrell and Robins (1982b) and extended the analysis to higher-order statistical moments and the shape of the one-point concentration PDF. These experiments have also been replicated numerically, most notably using Large Eddy Simulations (LES), by Xie et al. (2007), who focused on extreme concentration values for both elevated and ground-level sources, by Ardeshiri et al. (2020), who investigated the mechanisms generating concentration fluctuations, and by Cassiani et al. (2024), who analyzed the production, transport, and dissipation of concentration fluctuations, as well as the modeling of their one-point PDFs. This combined body of experimental and numerical works on scalar dispersion over flat terrain consistently indicates that the gamma distribution provides the most suitable model for the concentration PDF across a wide range of distances from the source, for both elevated and ground-level releases. However, the accuracy of the gamma distribution declines both near the source (Yee et al., 1993a) and at the plume edges (Lim and Vanderwel, 2023), where the lognormal distribution has been found to provide a better fit to experimental concentration PDFs. Moreover, its ability to capture the upper tail of the concentration PDF has been questioned by several authors (Efthimiou et al., 2016). In such cases, alternative distributions, such as the exponential-tail (exponential) function, have shown improved performance (Talluru et al., 2017), particularly in the near-field region (Yee et al., 1994). As an alternative to the gamma distribution, some studies have explored the use of the Weibull distribution (Lung et al., 2002; Oettl and Ferrero, 2017), which offers the notable advantage of providing an analytical formulation for the PDF percentiles. This feature has practical relevance, particularly for predicting peak-to-mean concentration ratios, an important consideration in applications such as odor impact assessment (Oettl and Ferrero, 2017). While the Weibull distribution captures key features of concentration statistics, it generally reproduces the full PDF with slightly less accuracy than the gamma distribution. A notable exception is the water channel study by Yee et al. (1993b), which found the Weibull distribution to outperform the gamma distribution. This discrepancy may be attributed to the fundamentally different flow regime in that experiment, which involved a passive scalar with a Schmidt number of approximately 830, around three orders of magnitude higher than values typical of atmospheric pollutant dispersion.

Apart from the many studies focusing on terrains with a uniform low roughness, fewer experimental works aimed at determining the effects of the built environment on the statistics of concentration fluctuations. Most of them are dedicated to urban environments (Ono and Nozu, 2024; Melo et al., 2023; Gailis and Hill, 2006; Gailis et al., 2007; Hsieh et al., 2007), at the scale of a neighborhood (Bi et al., 2025; Pearce and Baker, 1999) or a street canyon (Andronopoulos et al., 2001). Gailis and Hill (2006) and Gailis et al. (2007) reproduced the MUST (Mock Urban Setting Test, Yee and Biltoft, 2004) field experiment in a wind tunnel and a water channel, and validated the gamma distribution in these conditions. They also observed the broadening of the plume close to the source due to the wakes of obstacles. In such regularly spaced obstacles configurations, thermal stratification of the boundary layer impacts both plume shape and maximum concentration levels (Marucci and Carpentieri, 2020). Simpler cases containing only one single element proved the effect of both obstacle shape and height on the velocity field and, hence, on the concentration field (Mavroidis et al., 2015).

Notably, Salizzoni et al. (2025) characterized the dispersion from a line source downwind of a single obstacle, and tested the accuracy of the lognormal and the gamma distributions respectively inside and outside the recirculating region. However, the relevance of modeling the concentration PDF with a gamma distribution was questioned in more complex geometries, particularly in street canyons (Papp et al.,

2024; Del Ponte et al., 2024). Notably, Del Ponte et al. (2024) showed the lognormal model to be more adapted to model the PDF of a scalar released by a line source. The gamma distribution is however an accurate predictor of high percentiles of concentration within urban geometries (Efthimiou et al., 2016; Oettl and Ferrero, 2017), similarly to the Weibull model, which can be considered as an analytically convenient variation of the former.

Complex industrial environments and realistic urban district configurations (Ono and Nozu, 2024; Arnold et al., 2004; Carpentieri et al., 2012), which are both marked by dense and complex built structures, are even more rare, and there is a lack of knowledge about which model best suits the distribution of concentration in these particular geometries. Indeed, most studies considering the effect on pollutant spread of complex built elements typical of production plants do not consider concentration fluctuations at all. To fill this gap, in this work we therefore focus on the atmospheric dispersion of a passive scalar on a realistic industrial site. We first characterize the velocity field induced by the numerous obstacles (Section 3), while varying the geometry of the upstream building. The concentration field is analyzed in Section 4. We first assess the impact of the site geometry on the mean (Section 4.1) and standard deviation (Section 4.2) of the concentration field. Then, we focus on the one-point probability density function of concentration in Section 4.3. We compare the experimental distributions of concentration to the gamma, 2-parameters Weibull and lognormal distributions, which are the most validated models in the literature. To conclude, we analyze concentration peaks and percentiles.

## 2. Wind tunnel setup

The experiments took place in the atmospheric wind tunnel at the Ecole Centrale de Lyon, France. This is a recirculating wind tunnel of dimensions  $14\text{ m} \times 3.7\text{ m} \times 2\text{ m}$  apt to simulate flows reproducing the dynamics of a neutral atmospheric boundary layer. This is achieved by combining the effect of a turbulence grid and Irwin spires (Irwin, 1981), placed at the entrance of the test section, and roughness elements distributed over the entire wind tunnel floor. In this study, the wind tunnel set up adopted to reproduce this boundary layer flow is the same as that presented and analyzed by Nironi et al. (2015). We obtain a fully turbulent flow imposing a free stream velocity  $U_\infty = 5.0\text{ ms}^{-1}$ , the boundary layer height is  $\delta_{BL} = 0.8\text{ m}$  and the Reynolds number  $Re = U_\infty \delta / \nu = 2.65 \times 10^5$ , where  $\nu = 1.51 \times 10^{-5}\text{ m}^2\text{ s}^{-1}$  is the air kinematic viscosity at  $T = 20^\circ\text{C}$ .

The boundary-layer flow encounters a group of obstacles designed to replicate the key geometric features of a real industrial site. The characteristic height of the blocks representing the site is an order of magnitude smaller than the depth of the boundary layer  $\delta_{BL}$ . This configuration allows the wind tunnel experiment to capture the characteristic scale separation between the larger atmospheric eddies, whose size scales with  $\delta_{BL}$ , and the smaller vortices shed in the wake of the reduced-scale buildings.

A single wind direction was investigated. The approaching flow first encounters a tall building, followed by a group of columns representing storage tanks, and two long cuboids. The remainder of the site consists of smaller obstacles arranged to form an inner open space resembling a courtyard that contains additional tanks (see Fig. 1). Although the buildings have simplified geometries compared to those in real industrial sites, the model effectively captures the diversity of scales and spatial layouts typical of facilities such as refineries, chemical plants, and steelworks.

One of the focuses of our investigation is to assess the impact of complex structures, such as intertwined pipes and tanks, commonly found on industrial sites, on pollutant dispersion. We represent these elements collectively as a single porous obstacle that captures the overall aerodynamic influence of such scaffolding. To evaluate how obstacle porosity affects the flow and dispersion across the site, the upwind building is modeled in three different configurations (see Fig. 1):

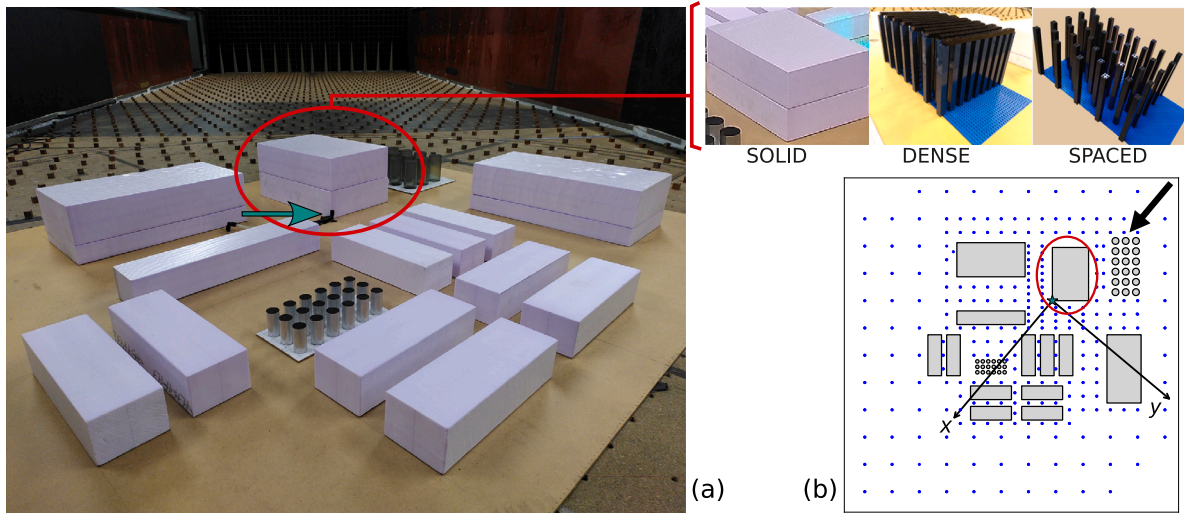


**Fig. 1.** **a** Small-scale model of the idealized industrial site in the wind tunnel where velocity and concentration measurements were performed. The source (shown by the green arrow), is placed at the corner of the highest building of the site. The entrance of the wind tunnel, with the grid, Irwin spires and roughness elements are visible in the background. The highest building (of height  $\delta$ , circled in red) is replaced by the porous elements on the top right corner. **b**  $x$  and  $y$  axes (shown with a length of  $6\delta$  with the origin at the source position) and velocity measurement points. The incoming wind direction is indicated by the black arrow.

1. a solid parallelepiped, referred to as ‘solid’;
2. a densely packed array of columns, referred to as ‘dense’;
3. a sparse array of rectangular columns, referred to as ‘spaced’.

The ‘dense’ and ‘spaced’ configurations have solid volume fractions of 0.24 and 0.1, respectively, and are used as alternatives to the ‘solid’ configuration in the wind tunnel experiments (see Fig. 1(a)).

A source of ethane of diameter 8 mm is placed at the corner of the upwind building, as shown by the green arrow in Fig. 1. Ethane has the same density as air, which is why it was chosen to simulate a neutrally buoyant pollutant.

We define the horizontal axes  $x$  (along the mean wind direction) and  $y$  (perpendicular) as shown on Fig. 1(b), the vertical axis  $z$ , and the velocity components  $u$ ,  $v$  and  $w$  respectively along  $x$ ,  $y$  and  $z$ . In the following, positions on the site indicated by ‘left’ and ‘right’ will refer to the left hand side and right hand side of the considered image, for simplicity. Distances are normalized by the height of the upwind building on the site ( $\delta = 0.192$  m), while velocities are divided by the velocity at the top of the boundary layer,  $U_\infty$ . Dimensionless quantities are indicated by the \* symbol.

Velocity measurements were performed with a Laser Doppler anemometer (LDA). Two 5 W power lasers of respective wavelengths 488 nm and 514.5 nm were used to measure simultaneously two components of velocity. Each laser generated two beams of diameter 0.1 mm crossing at the measurement point and forming a measurement volume of dimensions about 0.1 mm  $\times$  0.1 mm  $\times$  2 mm. A mirror was used to redirect the beams for measurements on the vertical plane. Aerosol seeding particles of diameters between  $0.5 \times 10^{-6}$  m and  $2 \times 10^{-6}$  m were used and the average acquisition frequency was around 1550 Hz. Acquisition lasted until at least 200000 particles were detected, in order to obtain reliable statistics, notably the mean and variance of velocity.

Ethane concentration was measured with a fast flame ionization detector (FFID) (Fackrell, 1980). The apparatus was placed above the measurement point where air was sucked through a 0.3 m long sampling tube and driven towards the instrument which response frequency reached approximately 800 Hz (Nironi et al., 2015). The instrument voltage ranged from 0 to 10 V corresponding to volumetric concentrations between 0 and 5000 ppm by a linear relation. The instrument was calibrated twice a day using air–ethane mixtures of known concentrations, respectively of 0, 500, 1000 and 5000 ppm. Since the wind tunnel is a closed-circuit system, the concentration increased during the measurement period and the background concentration had to be

measured before and after measuring each point and removed from the signal. Measurements lasted for 300 s, ensuring the convergence of the first four order moments of concentration statistics.

To avoid saturation of the FFID during measurements close to the source, ethane was diluted with air, maintaining a global mass flow rate at the source of  $0.5 \text{ L min}^{-1}$ .

Dimensionless concentrations are calculated from the mass concentration  $C$  as  $C^* = C/\Delta C$  (Nironi et al., 2015), with  $\Delta C = Q/(U_\infty \delta_{BL}^2)$ , where  $Q$  is the mass flow rate of ethane at the source.

### 3. Velocity field

This section is dedicated to the analysis of the velocity field in the three configurations: ‘solid’, ‘dense’ and ‘spaced’, with a focus on the recirculation zone generated by the upwind building.

Fig. 2 shows the mean velocity field measured over two horizontal planes. The presence of the upwind building gives rise to a recirculating region, whose position is impacted by the building porosity, which also affects the velocity decrease within the wake. For the ‘solid’ configuration (Fig. 2(a)), a strong current develops along the left edge of the building (negative  $y$  values) at  $z^* = 0.26$ , displacing the recirculation zone towards positive  $y$  values. At the upper layer  $z^* = 0.78$  (Fig. 2(b)), a weaker counter-current appears from right to left within the same corridor, but the flow remains mainly aligned with the forcing wind direction. This enlightens that, as expected, the ‘solid’ configuration has a strong blocking effect which highly perturbs the flow. Conversely, the ‘dense’ configuration (Fig. 2(c) and (d)) generates a wider recirculating region that extends more towards negative  $y$  values, showing smaller velocities compared to the ‘solid’ case. Finally the ‘spaced’ configuration has the weakest impact on the velocity field. It does not generate a recirculation zone, as visible in Fig. 2(e) and (f), the norm of velocity attains values very close to those of the upwind flow, and the wind direction is only minimally impacted by the presence of the spaced columns.

Fig. 3(a)–(f) presents horizontal profiles of the norm of the mean velocity components  $u$  and  $v$  along the downwind sections shown in Fig. 2. Similarly, Fig. 3(g)–(l) reports the profiles of the velocity variance  $1/2(u'^2 + v'^2)$ . In the following we refer to this quantity as turbulent kinetic energy (TKE), acknowledging that a complete computation would also require the contribution of the vertical component  $w'^2$ . The shift to the right-hand side of the recirculating region in the ‘solid’ case

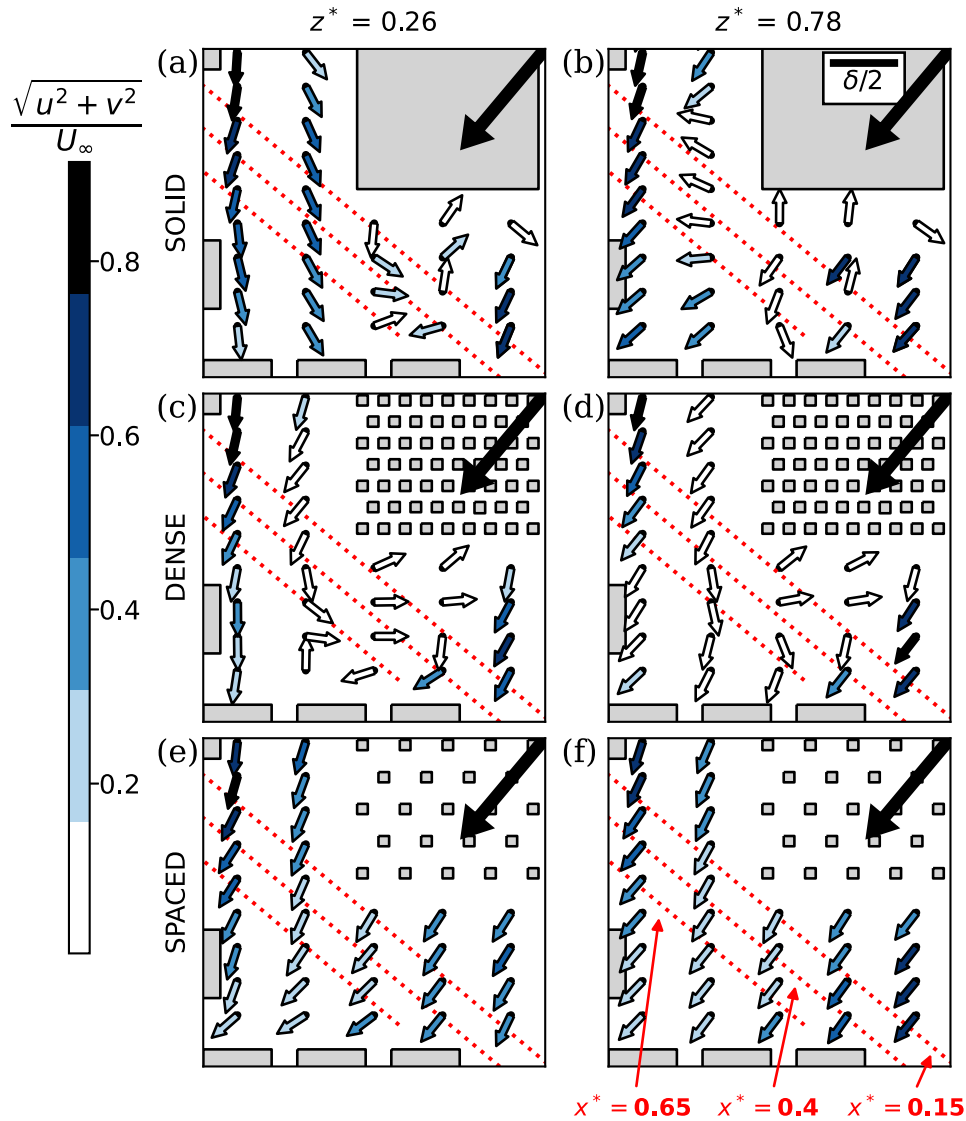


**Fig. 2.** Maps of dimensionless mean velocity, considering components along  $x$  ( $u$ ) and  $y$  ( $v$ ) for two horizontal slices for the three configurations. **a–b:** ‘solid’, **c–d:** ‘dense’, **e–f:** ‘spaced’. Black arrows show the forcing wind direction, the scale is shown on the top right corner. Recirculation is clearly visible in the ‘solid’ and ‘dense’ configurations, but the forcing wind direction stays predominant in the ‘spaced’ configuration. Diagonal lines with their corresponding distances to the source indicate positions of horizontal profiles of Fig. 3.

corresponds to a strong reduction of mean velocity (Fig. 3(a) to (f)), which reaches its minimum at higher  $y^*$  values than in the other configurations. The ‘dense’ case exhibits the lowest velocity levels in most of the building wake, due to the effect of densely packed columns, but the ‘solid’ configuration reaches locally comparable velocity levels at the minimum of the depletion. Turbulent kinetic energy levels (shown in Fig. 3(g) to (l)) have stronger variability in the ‘solid’ configuration than in other cases, and TKE is globally highest and lowest in the ‘solid’ and ‘spaced’ cases, respectively.

#### 4. Concentration field

In this section, we first characterize the concentration field over the whole site for the three cases. We analyze the effect of the upwind building porosity on statistics of the scalar concentration. The mean dimensionless concentration ( $C^*$ ) and fluctuation intensity ( $i_c = \sigma_c/C$ ) are shown on horizontal slices at two heights ( $z^* = 0.16$  and  $z^* = 0.47$ ) and on vertical profiles (which horizontal positions are shown in Fig. 4 with special marker shapes) for the three configurations. Subsequently, statistics of concentration fluctuations are investigated more closely for

the ‘solid’ case, with a focus on the PDF of the one-point concentration, on its high order statistical moments, and peak to mean ratios. We test several model distributions against the experimental concentration data to determine which model is the most accurate predictor of concentration fluctuations.

##### 4.1. Mean concentration field

Fig. 4 shows locations of the concentration measurement points at ground level (panels a, d, g) and mid-height (panels b, e, h) for the three configurations. The points are arranged in a spatial grid, which enables a clear identification of the pollutant plume. Locations of the vertical profiles shown on Fig. 4(c), (f) and (i) are chosen in order to capture the plume behavior at this distance from the source (the exact location of the points vary therefore from a case to another). Three main distances are targeted, a first one close to the source inside the porous building wake, a second one further in the mid-field inside the group of small buildings, and a last one in the far field downwind of the whole site.

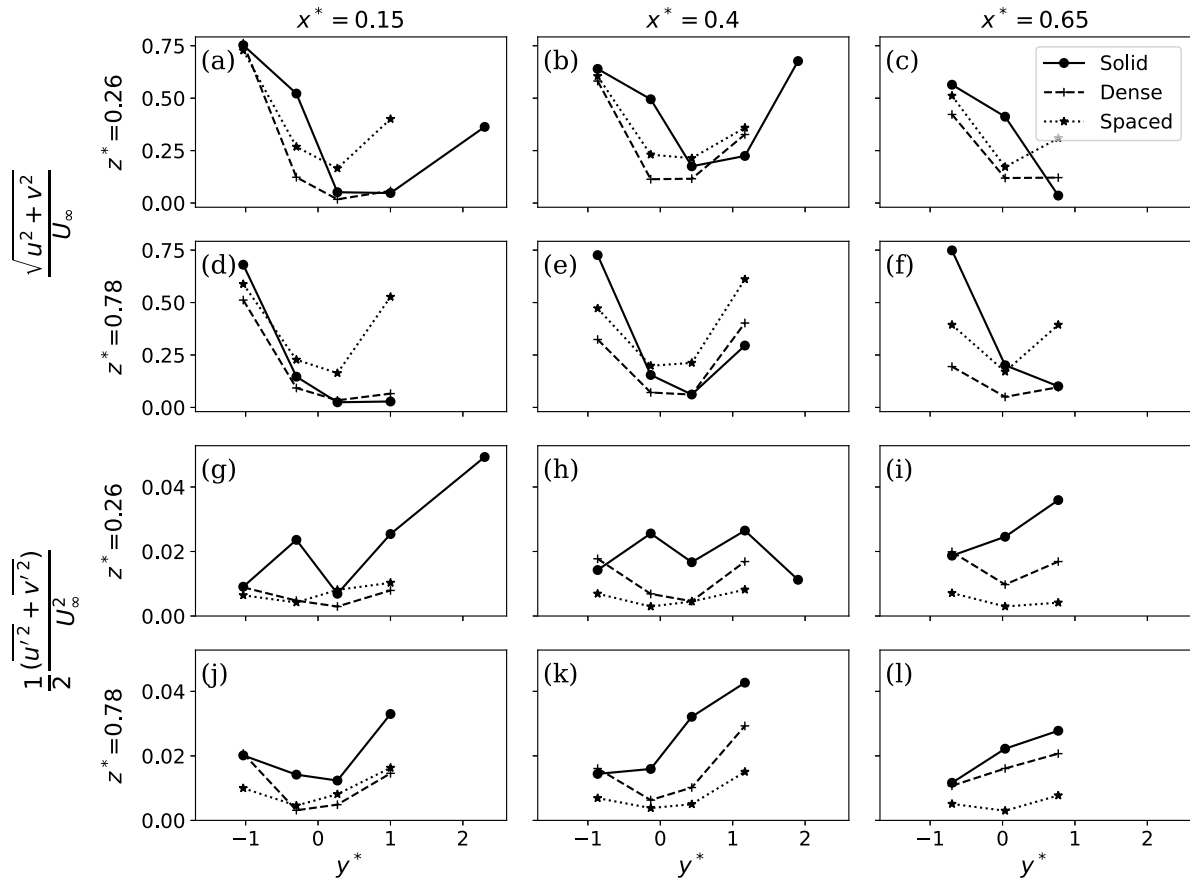


Fig. 3. Norm of mean velocity (panels a to f) and turbulent kinetic energy (panels g to l) along the diagonals downwind of the porous building shown in Fig. 2, computed from the two horizontal velocity components  $u$  and  $v$  only. Both shape and intensity of the wind field are affected by the upwind elements.

The impact of the site configuration on the mean concentration field is visible mainly in the shape of the plume spread, as shown on the maps of Fig. 4(a)–(b), (d)–(e) and (g)–(h). In the ‘solid’ configuration (Fig. 4(a)–(b)) the plume is shifted to the right-hand side of the wake. This is a consequence of the velocity field shown in Fig. 2. Downwind, the plume spreads throughout the whole group of buildings. In the ‘dense’ configuration (Fig. 4(d)–(e)), the plume is initially located much closer to the corner of the porous building, due to the shape of the recirculation. This feature is still visible in the midfield, since the plume is located towards more negative  $y^*$  values compared to the ‘solid’ case. Finally, in the ‘spaced’ configuration (Fig. 4(g)–(h)), the plume is much narrower, it is elongated along the forcing wind direction, and exhibits higher mean concentration values. It covers mainly the empty space in between the small buildings (‘courtyard’) instead of the group of small buildings.

The vertical profiles on Fig. 4(c), (f) and (i) show that the mean concentration field is affected by the porosity of the upwind building. Profiles close to the source in the ‘solid’ case reach a maximum around  $z^* = 0.6$  (Fig. 4(c)). Concentration values over and below this height decrease almost symmetrically to reach similar concentration levels at the top of the building as at the ground. The tracer is thus carried by the recirculation and diluted more actively at mid-height of the building wake.

In contrast, close to the source the profiles of mean concentration in the ‘dense’ case are much more homogeneous vertically (Fig. 4(f)). The tracer gas is diluted over almost the whole volume of the wake, which generates lower concentration levels at mid-height of the building with respect to the ‘solid’ case. However, zones that contain mainly pure air

in the ‘solid’ case are reached by the plume in the ‘dense’ configuration, notably close to the ground.

The ‘spaced’ configuration has the opposite behavior (Fig. 4(i)). The plume is narrower and the maximum mean concentration is reached below  $z^* = 0.6$ , i.e. below the height of maximum mean concentration in the ‘solid’ case. This is a consequence of the low impact of columns on the velocity field. As a result, the plume exhibits a dispersion pattern similar to that observed in the absence of an upwind obstacle.

Differences in the shapes of vertical concentration profiles reflect in the values of maximum concentration and their positions on the first circle, flatter profiles being linked to lower concentration maxima. The maximum concentration values recorded on the first circle at  $z^* = 0.16$  are  $\bar{C}^* = 367.9$  in the ‘spaced’ case (at plume center),  $\bar{C}^* = 135.6$  in the ‘solid’ case (close to the bottom right corner of the upwind building), and  $\bar{C}^* = 111.5$  in the ‘dense’ case (at the entrance of the corridor most to the right within the group of buildings). This is due to strong wakes generated in the ‘solid’ and ‘dense’ configurations that dilute the plume and displace its center of mass.

These differences, that are highly visible in the short range, tend to fade at larger distances from the source. The main differences in the mid range are the higher values of mean concentration reached in the profile of the ‘spaced’ case (Fig. 4(i)), compared to the other site configurations (Fig. 4(c) and (f)). The maximum mean concentration attained in the ‘spaced’ configuration on the second circle still is 3 times higher than the maximum of ‘dense’ and ‘solid’ configurations, and it is reached at the plume centerline close to the tanks.

In the far field, the main noticeable difference between configurations is the position of plume maximum, which is still shifted towards positive values of  $y^*$  in the ‘solid’ and ‘dense’ cases (see

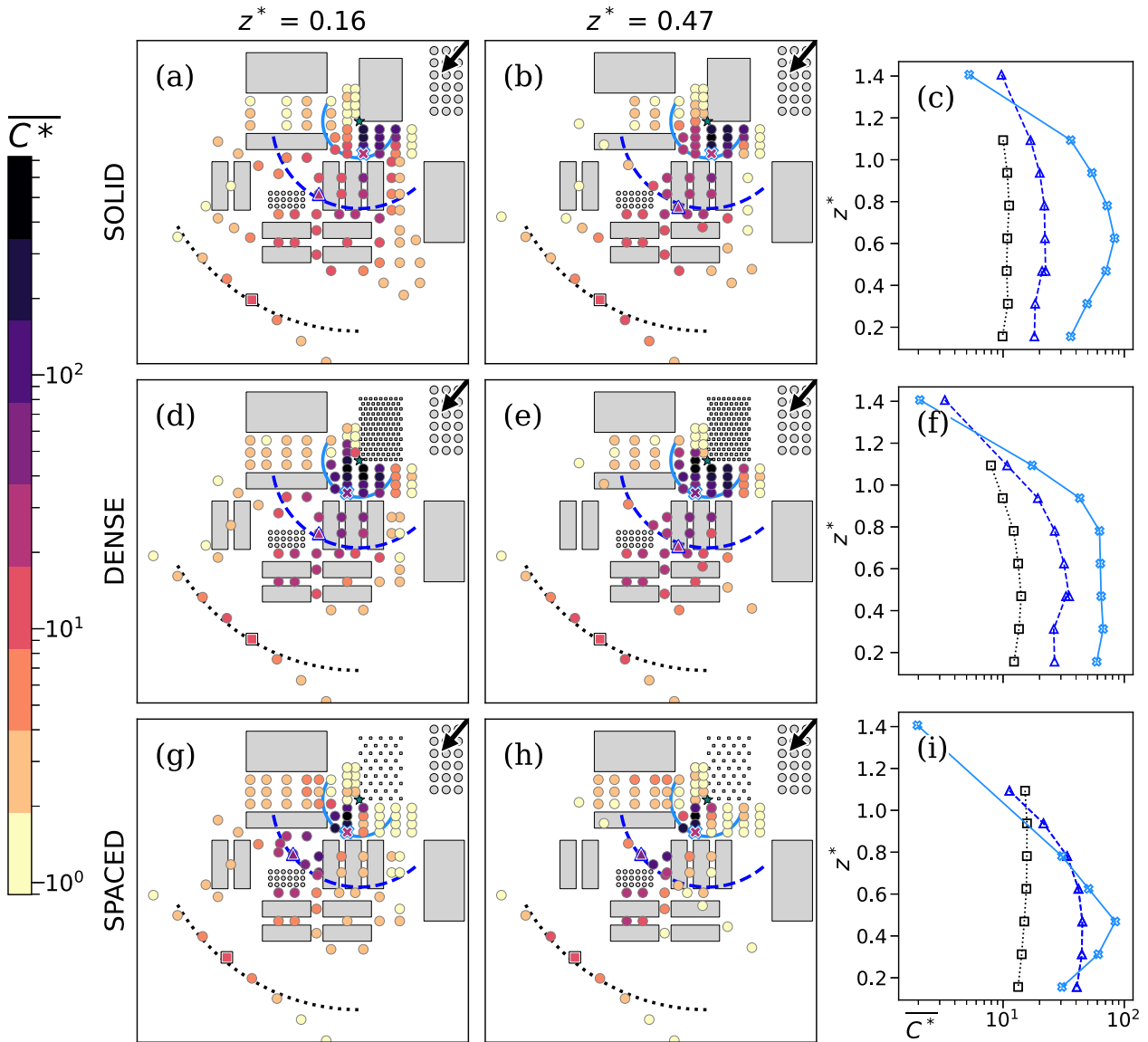


Fig. 4. Average dimensionless concentration ( $\overline{C^*}$ ) on 2 horizontal slices (panels a–b, d–e and g–h) and 3 vertical profiles (panels c, f and i) for the 3 configurations. Positions of vertical profiles (shown as cross, triangle and diamond markers on the maps) were chosen according to their distances to the source (circles of corresponding colors). For the middle range, vertical profiles were split into a lower and an upper layer where the presence of buildings rendered it necessary. The source is placed at the corner of the upwind building (green star) and the black arrows indicate the forcing wind direction. Both plume shape and extent are impacted by building porosity.

Fig. 4(a)–(b), (d)–(e) and (g)–(h)). The maximum mean concentration values measured in this region are similar between all three configurations, considering the scarce spatial resolution available in the data. However, this spatial resolution in the far field is sufficient to observe the shift of the plume centerline in the ‘solid’ and ‘dense’ cases with respect to the ‘spaced’ configuration. There is therefore a global effect of the building porosity not only on its wake but also on the spread of the entire plume downwind.

#### 4.2. Intensity of the concentration fluctuations

We evaluated the fluctuation intensity  $i_c = \sigma_c / \overline{C}$  and investigated how it is impacted by the building configuration (Fig. 5).

The highest values of  $i_c$  are reached on the first circle in the ‘solid’ and ‘spaced’ configurations, contrary to the ‘dense’ configuration, in which  $i_c$  is up to two times smaller. Profile shapes are also impacted,

as shown on Fig. 5(c), (f) and (i) where the minimum of  $i_c$  is reached around  $z^* = 0.6$  in the ‘dense’ case (Fig. 5(f)). The particularly low values of  $i_c$  visible for the first circle in Fig. 5(f) correspond to an almost flat mean concentration profile for the first circle in Fig. 4(f), which indicates a more efficient mixing in the dense configuration close to the source compared to the other configurations. As shown on Fig. 5(i), fluctuation intensity also reaches a slight minimum in the ‘spaced’ case, at the altitude of the maximum of the corresponding mean concentration profile. This is closer to the typical behavior of a passive scalar plume over flat terrains (Nironi et al., 2015). On the contrary, in the ‘solid’ configuration, close to the source,  $i_c$  exhibits higher values close to the ground, as shown in Fig. 5(c). Fluctuation intensity at the top of the building is clearly smaller than below  $z^* = 0.6$ , meaning that the ‘solid’ configuration results in weaker mixing compared to the ‘dense’ configuration, which is associated with stronger fluctuations within the building wake in the solid configuration. The least efficient

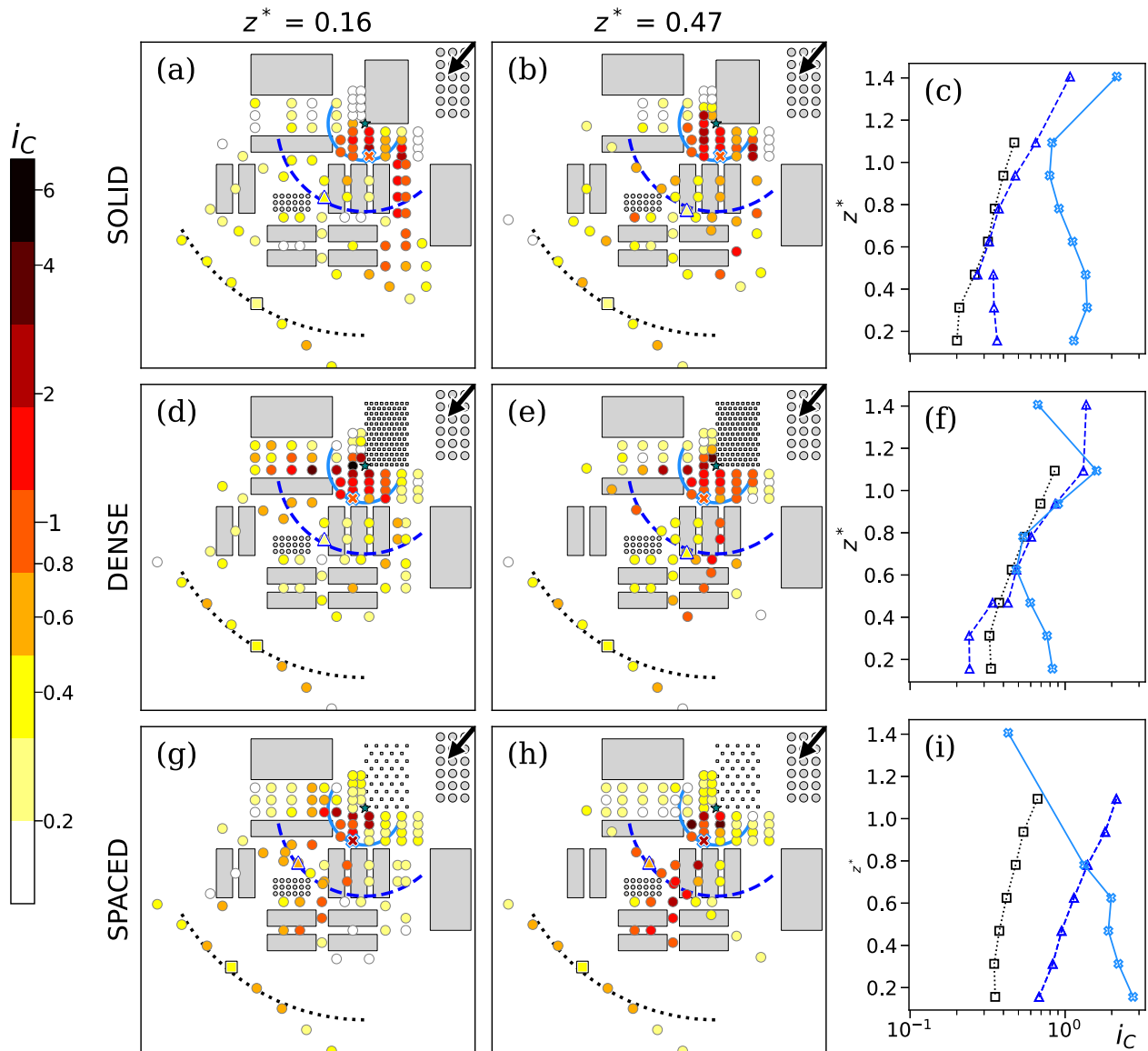


Fig. 5. Intensity of concentration fluctuations. Same structure as Fig. 4. Fluctuations are higher in the recirculation zone close to the source for all configurations, on the sides of the group of small buildings (plume borders) for the ‘solid’ case, and at plume borders for other configurations.

mixing is observed in the ‘spaced’ configuration (Fig. 5(i)), for which vertical profiles of fluctuation intensity show higher values than other configurations at all distances from the source.

Nevertheless, scalar dispersion is influenced not only by the upwind obstacle but also significantly by the smaller elements located downwind. Within the group of downwind buildings in both the ‘solid’ and ‘dense’ cases (see Fig. 5(a), (b), (d) and (e)), the mean concentration is spatially homogeneous. However,  $i_c$  is impacted by the local geometry, and reaches high values on the right side (positive  $y^*$  values) of the group of small buildings in the ‘solid’ configuration (Fig. 5(a)). In contrast, inside most of the corridors between buildings fluctuation intensity remains below 0.5 in both ‘solid’ and ‘dense’ configurations (see Fig. 5(a) and (d)). In the ‘dense’ case at  $z^* = 0.47$  (Fig. 5(e)), a line of larger values of  $i_c$  is visible, which corresponds to the plume border, where values of  $\sigma_C$  exceed those of  $\bar{C}$ . A similar pattern is observed in the ‘spaced’ configuration (see Fig. 5(g) and (h)), where the fluctuation intensity locally exceeds 1 at the plume boundary within the group of small buildings. Thus, in both the solid and dense configurations, the

local geometry of the mid-field building cluster affects  $i_c$  more strongly than it affects  $\bar{C}^*$ . These obstacles, that are smaller than the upwind building, tend to homogenize and widen the plume, but their effect on concentration fluctuations is more local.

#### 4.3. PDF of one-point scalar concentration

We present a comparison between experimentally measured concentration distributions and several theoretical models for the one-point concentration PDF. Our objective is to identify the model that most accurately captures the statistics of concentration fluctuations within a complex site. All results are shown for the ‘solid’ configuration only, which generates the most turbulent wake. In this configuration, the group of small buildings downwind of the source is entirely covered by the plume. We eliminated points with a low signal to noise ratio. Practically, this implied, as in Andronopoulos et al. (2001), that we removed only measurement points with an average concentration below 10 ppm. We test the gamma, 2 parameter Weibull (2p-Weibull)

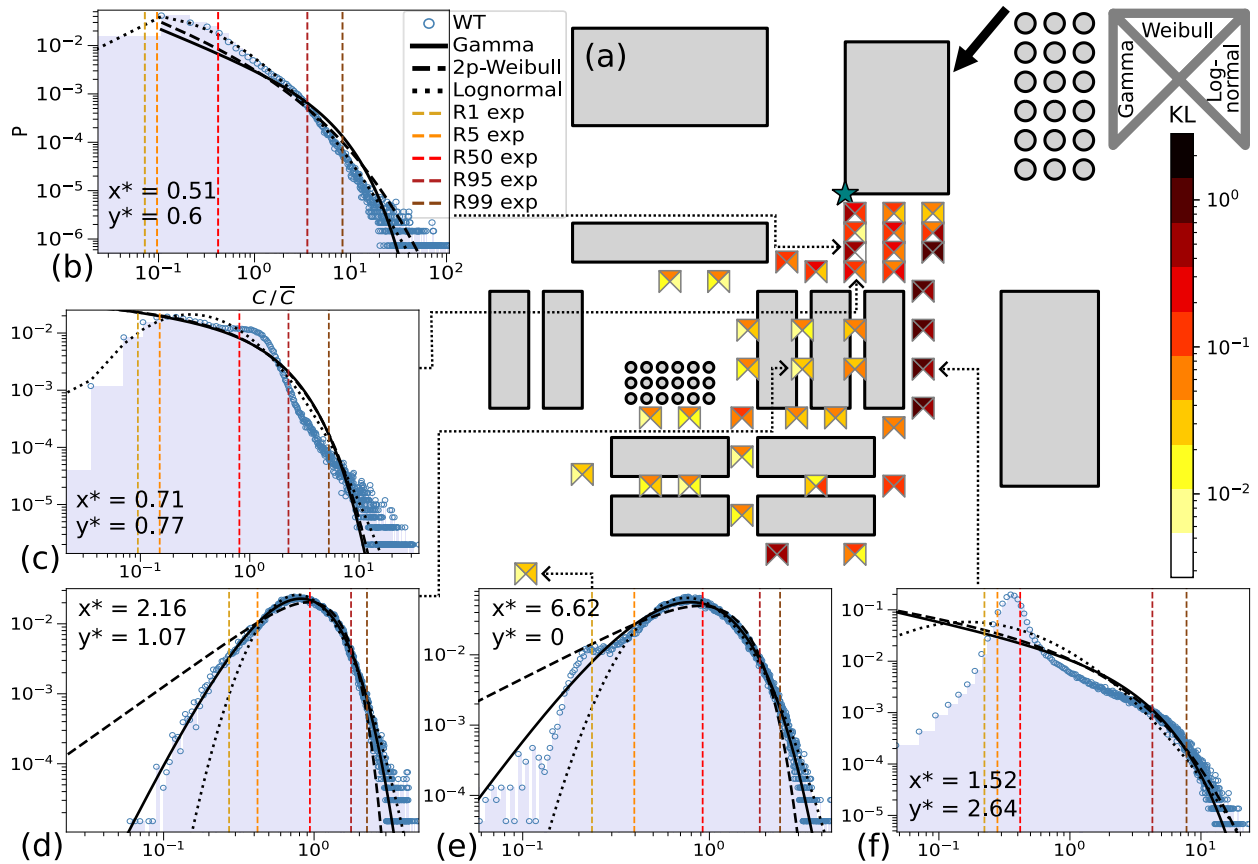


**Fig. 6.** Kullback–Leibler divergence (KL) at ground level (panel a) and distributions of concentration values at particular points (panels b–f). Ratios of first, 5th, 50th, 95th and 99th percentiles to the mean value (R1 to R99) are shown on the PDF. On the map (panel a), the KL values of the gamma, 2p-Weibull and lognormal distributions are shown as triangles respectively on the left, top and right of the point location.

and lognormal distributions, which are the most validated models in the literature (Cassiani et al., 2020). Mathematical details about these distributions are provided into Appendix A.

As a measure of the agreement between the model and the experimental distributions of concentration values in the time series, we consider the Kullback–Leibler (KL) divergence (see Appendix B). Smaller KL values correspond to a better model-data agreement. Fig. 6(a) shows a map of KL values at the lowest measurement layer ( $z^* = 0.16$ ) with some examples of experimental concentration distributions compared to model PDFs (Fig. 6(b)–(f)). The horizontal layer shown in Fig. 6(a) lies below the height at which the plume reaches its maximum mean concentration. Nevertheless, it remains highly relevant, as the majority of risks associated with pollutant dispersion concern human exposure near ground level.

In Fig. 6, examples of one-point experimental and modeled distributions of concentration are shown at key places on the site. All distributions perform better in the group of small buildings, rather than on the right side of the group of buildings (Fig. 6(a)), i.e. at the plume border, characterized by high  $i_c$  values. We observe complex shapes of the statistical distributions, likely resulting from the convolution of simpler distributions, induced by the merging of pollutant puffs transported along different paths.

KL values are higher in the wake of the tallest building, except on the left (negative  $y^*$  values) side of the wake for the lognormal model. In this zone the lognormal distribution suits better to experimental data than the gamma and 2p-Weibull models, at all heights (not shown on Fig. 6). Nevertheless, over the group of small buildings, better KL values

are obtained by the gamma model. These results are in accordance with those of Salizzoni et al. (2025), who modeled the PDF of a scalar emitted by a line source with a lognormal distribution in the wake of a single obstacle, and with a gamma distribution further from the source. Below and over the height of the small buildings, respectively, the lognormal and the 2p-Weibull distributions are almost as accurate as the gamma model. In the far field, KL values of the 2p-Weibull model are slightly lower (meaning better) than other distributions.

The best model distribution hence varies with the distance to the source and the local impact of geometry. The lognormal distribution is more appropriate in the wake of the tallest building, while the gamma distribution is more accurate in the mid range, even in the presence of grouped obstacles perturbing the flow. This extends the already-known validity of the gamma model over flat terrains (Cassiani et al., 2020) to built environments. Finally, the 2p-Weibull model performs better in the far field. Regions where the geometry has a strong impact, particularly at plume border, present high KL values for all distributions. However, it is important to notice that KL values computed over the whole PDF of concentration reflect the agreement for both small and high concentration levels with respect to the mean, which are not necessarily linked. For example on the side of the group of small buildings (Fig. 6(f)) the experimental concentration distribution has a very complex shape that is not captured accurately by the models below the 50th percentile, even though high concentration values are reasonably well reproduced, notably about the 95th percentile. To our knowledge, no such complex shapes were obtained at low concentration ranges in the few studies that describe the whole experimental

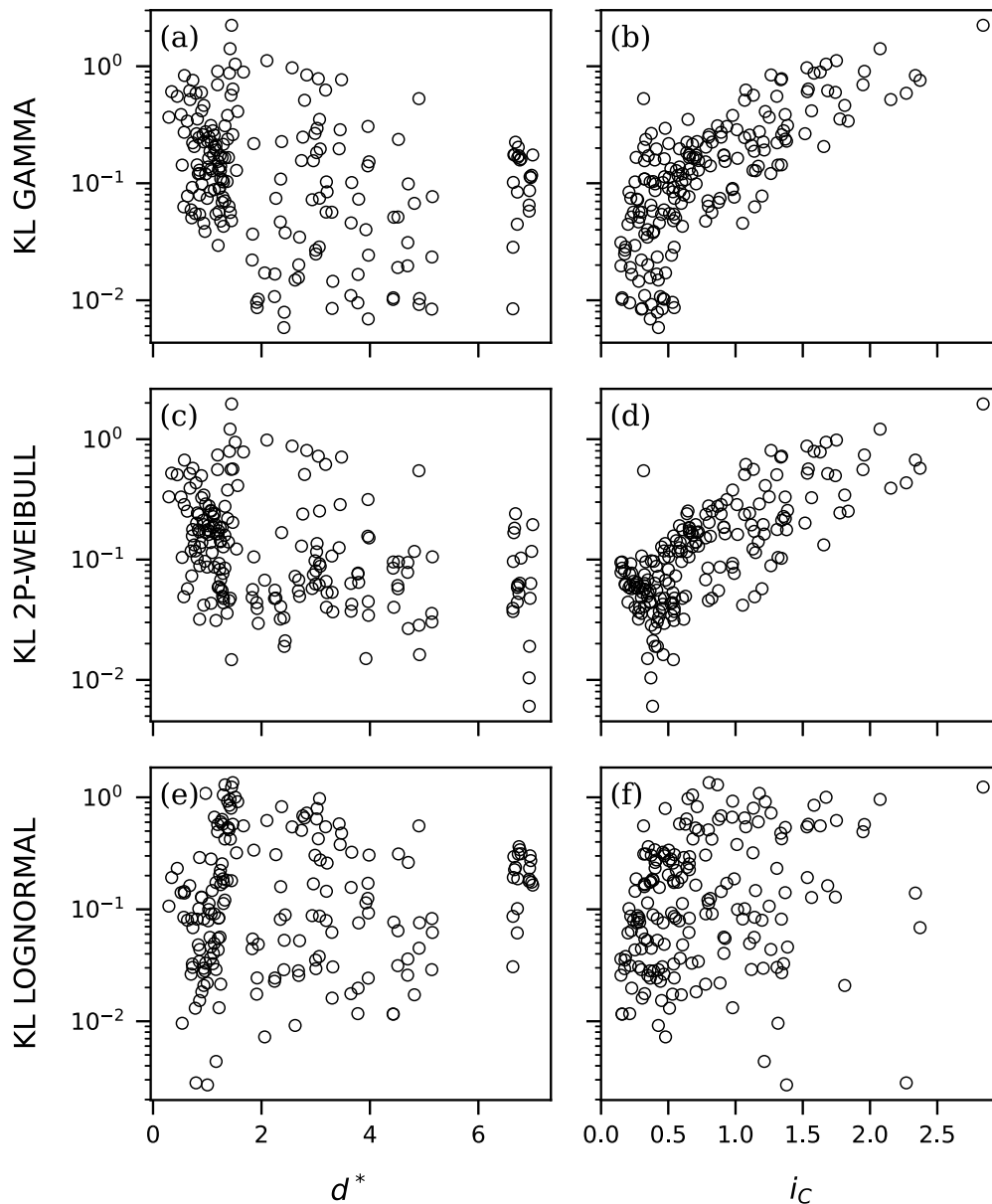


**Fig. 7.** Evolution of the Kullback–Leibler divergence, panels **a**, **c** and **e**: with the dimensionless distance to the source  $d^*$ , and panels **b**, **d** and **f**: with the concentration fluctuation intensity  $i_C$  for the gamma, 2p-Weibull and lognormal distributions. There is no clear dependence to the distance from the source but an evident link with the intensity of concentration fluctuations for the gamma and 2p-Weibull distributions. This link is not as patent for the lognormal distribution.

PDF of concentration obtained over complex terrains (which mainly concern street canyons, as [Del Ponte et al., 2024](#)). We suspect that the experimental PDFs result from the convolution of two or more simpler distributions, leading to a shape too complex to be accurately captured by the models tested.

In order to identify reliable predictors of the quality of agreement between model and experimental distributions, we plot the KL values depending on the distance from the source  $d^*$ , and the intensity of the concentration fluctuations  $i_C$  in [Fig. 7](#).

[Fig. 7](#) shows no dependence of KL values to the distance to the source ([Fig. 7\(a\)](#), [\(c\)](#) and [\(e\)](#)), but evidences a strong link with  $i_C$  for the gamma and 2p-Weibull models ([Fig. 7\(b\)](#) and [\(d\)](#)). The relation is much less evident for the lognormal distribution ([Fig. 7\(f\)](#)) since lower values of KL are reached even at  $i_C > 1$ . These points are mainly located inside the building wake, where, as showed previously (see [Fig. 6](#)), the lognormal distribution performs better than other models. The intensity of fluctuations of concentration can therefore be considered a good

indicator of the prediction of the PDF by the gamma and 2p-Weibull models. A high value of  $i_C$  corresponds to more intermittent signals, typically at plume border and close to the source, which is in agreement with the spatial distribution of KL values observed in [Fig. 6](#). Therefore, both the accurate prediction of high concentration levels and a reliable estimation of the overall PDF shape can be achieved based solely on the mean and variance of the concentration.

We focus on the concentration higher-order moments, peaks and percentiles. Higher order statistical moments, namely skewness and kurtosis, are computed from the three distributions and compared to the experimental quantities ([Fig. 8](#)), imposing the concentration mean and variance from experimental data (see [Appendix A](#)).

The gamma and lognormal models predict more accurately the skewness, compared to the 2p-Weibull model (see [Fig. 8\(a\)](#), [\(c\)](#) and [\(e\)](#)). The fraction of predictions within a factor of 2 of the observations is  $FAC2_G = 0.60$ ,  $FAC2_W = 0.38$ ,  $FAC2_L = 0.61$  for the gamma, 2p-Weibull and lognormal models respectively. Even though

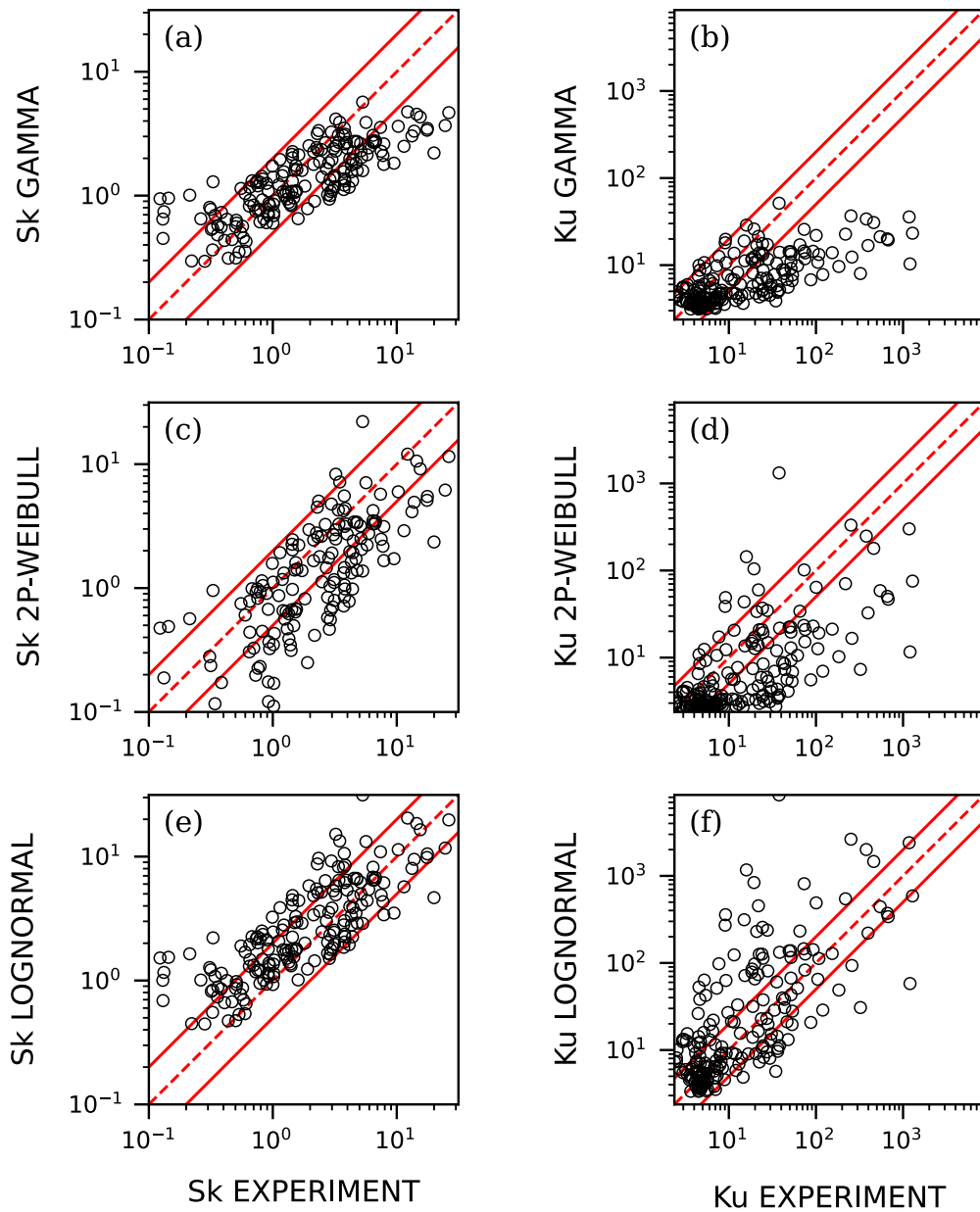


**Fig. 8.** Experimental **a**, **c** and **e**: skewness and **b**, **d** and **f**: kurtosis with respect to their modeled versions. Red lines correspond to a factor of 2 and 0.5 of the observations. Points with skewness values below 0.1 are not shown on the graphs (10 points for the gamma and lognormal cases, 40 points for the Weibull model over a total of 200 points). Skewness is predicted with a reasonable accuracy but kurtosis is badly captured. Gamma and lognormal distributions provide slightly better predictions than the 2p-Weibull model.

the lognormal and gamma distributions have a similar ratio of more accurate predictions, the positions of the points where these predictions perform better are different. Skewness values inside a factor of 2 are mainly located inside the group of small buildings for the gamma model whereas they are inside the wake of the upwind building for the lognormal model. Prediction of skewness by the 2p-Weibull model is worse than the gamma model within the group of small buildings but comparable elsewhere. Hence, the gamma distribution is a better predictor of skewness in the mid field while the lognormal distribution is more adapted in the recirculation zone in the near field, even though none of the three tested distributions provides satisfactory results in general.

Kurtosis is even more poorly estimated by the models (see Fig. 8(b), (d) and (f)) since fractions of prediction within a factor of 2 of the observations reach only  $FAC2_G = 0.60$ ,  $FAC2_W = 0.50$ ,  $FAC2_L = 0.53$ . Again, the gamma and lognormal models perform slightly better in the

mid and near field, respectively. The low quality of prediction of the high order statistical moments is mainly due to low concentration levels that are highly impacted by the local effects of the site geometry.

Although the tested model distributions may not perfectly reproduce the whole PDF of the experimental data (see Fig. 8), they capture the overall shape and, notably, peaks and percentiles (see Fig. 9).

Peak to mean ratios, estimated as the 95th, i.e.  $R_{95} = C_{95}/\bar{C}$ , and 99th percentiles, are presented in Fig. 9. The 95th (Fig. 9(a), (c) and (e)) and 99th (Fig. 9(b), (d) and (f)) percentiles are obtained from the model distributions in which the experimental mean and variance of concentration were imposed. They are then compared to the experimental percentiles.

All models are accurate for predicting peak to mean ratios, since all points lie within a factor of two. This demonstrates the capacity of all tested distributions to reproduce very high, and hence hazardous, concentration values. Contrary to Oetti and Ferrero (2017), we observe that

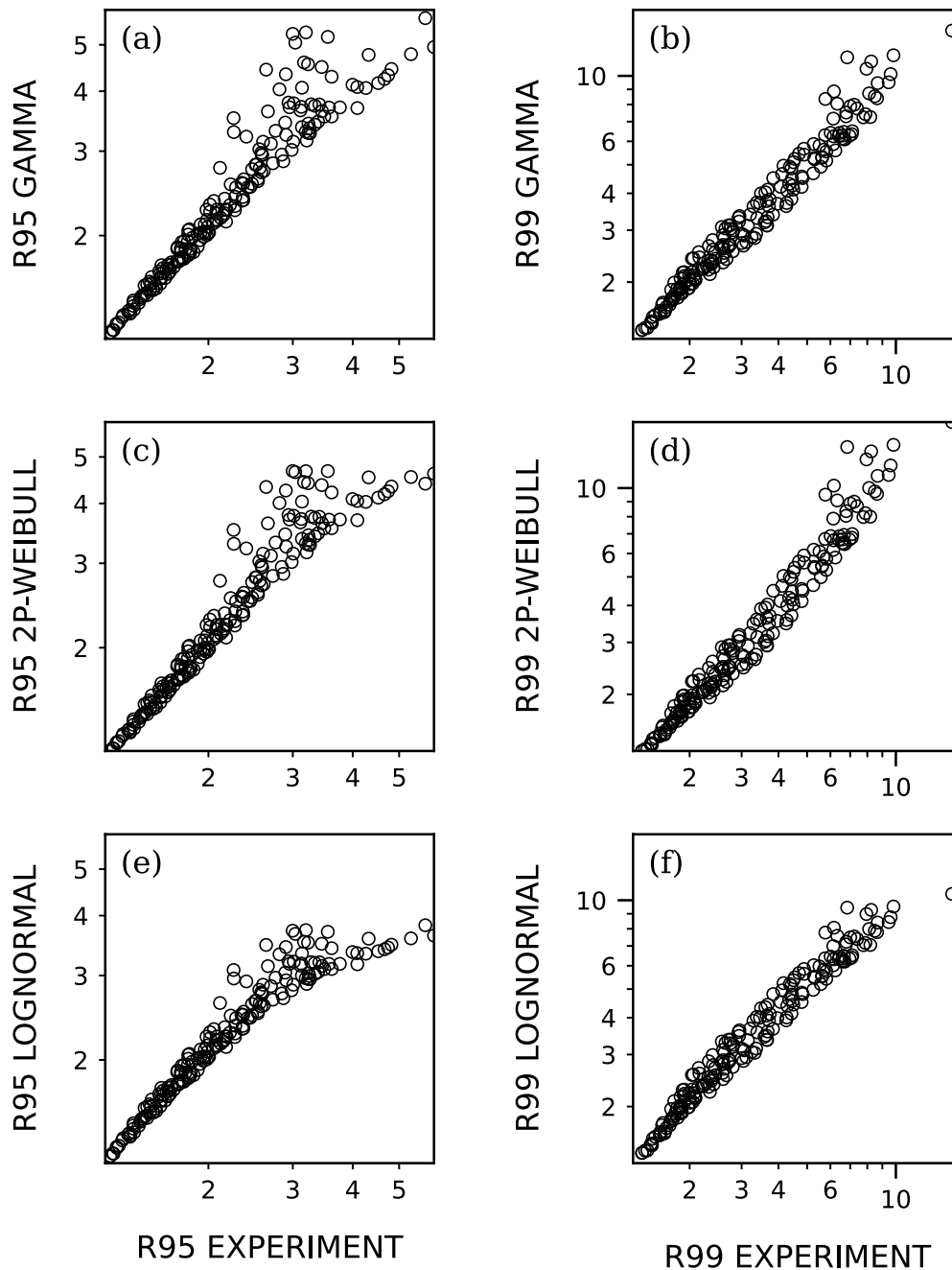


Fig. 9. Peak-to-mean ratios from a, c, e: the 95th and b, d and f: the 99th percentiles. Experimental values and predicted ratios from the 3 distributions are compared. All distributions provide excellent agreement with experimental data.

the performance of the gamma and the Weibull distributions are similar. Peak to mean ratios can hence be computed from high percentiles of the three models with a similar accuracy, and the analytical definition provided only by the 2p-Weibull model enables much faster computations (Oettl and Ferrero, 2017). It is much easier to obtain an accurate value of higher percentiles than the 3rd and 4th order moments of the distribution, which confirms the previous conclusions detailed over Section 4. Similar results were obtained by Papp et al. (2024) on completely different geometrical configurations, namely street canyons. The complex PDF shape that we observe could explain the difficulties encountered by Papp et al. (2024) into reproducing the kurtosis of concentration while high percentiles were accurately predicted by the gamma distribution.

## 5. Conclusion

This study investigates the dispersion of an airborne pollutant within an industrial site. We analyzed the velocity and concentration fields of a scalar released from a steady point source positioned at ground level, immediately downstream of the most upwind building of the site. The experiments involved modifying the site geometry by altering the configuration of the tallest upwind building. Specifically, this building was replaced with porous variants designed to simulate typical arrangements of pipes and tanks commonly found in real industrial environments.

The velocity field is significantly influenced by the configuration of the upwind building, with the solid (filled) version generating the most turbulent wake. In contrast, densely packed porous columns enhance mixing, while sparsely arranged columns primarily slow the flow

without creating recirculation zones. Consequently, the concentration fields are strongly affected by the upwind building configuration, with plume displacements due to porosity remaining evident even in the far field. The upwind element's impact on plume width and maximum concentration is most pronounced in the near and mid fields. Smaller obstacles tend to affect the concentration's standard deviation more than its mean, notably increasing fluctuation intensity when positioned at the plume edges.

We analyzed the statistics of one-point concentration fluctuations, focusing on modeling the concentration probability density function at varying distances from the release point. Following previous studies (Cassiani et al., 2020), we evaluated the gamma, two-parameter Weibull, and lognormal distributions. However, none of these distributions adequately captured the complex PDF shapes observed experimentally, which were influenced by the presence of obstacles. Notably, the lower half of the concentration PDF exhibited highly irregular shapes associated with elevated fluctuation intensity. Therefore,  $i_C$  serves as an indicator of the fit quality between the modeled and experimental concentration PDFs. Additionally, modeled skewness and kurtosis values showed considerable uncertainty, and no single distribution consistently represented the experimental concentration PDF across all distances from the source.

Despite these limitations, we identify model distributions that better fit the data depending on the distance from the source and the site region considered. Our results show that the lognormal distribution provides a more accurate fit in the wake of the upwind obstacle near the source, while the gamma distribution performs better in the mid field, even when grouped obstacles disrupt the flow. This finding extends the previously established validity of the gamma model over flat terrains (Cassiani et al., 2020) to built industrial environments. In the far field, the two-parameter Weibull distribution slightly outperforms the gamma model in describing the concentration PDF. Moreover, the quality of agreement between the model distributions and experimental concentration PDFs correlates with the fluctuation intensity particularly for the gamma and lognormal models.

Unlike lower concentration values, high percentiles are accurately captured by all three distributions across the entire site. This finding is particularly valuable for risk assessment in scenarios involving hazardous peak contaminant exposures, such as evaluating threshold exceedance and peak concentrations. For instance, it enables risk estimation based on numerical modeling outputs that provide both the time-averaged concentration and its variance.

### CRedit authorship contribution statement

**Claudia Schiavini:** Writing – original draft, Visualization, Investigation, Formal analysis, Data curation, Conceptualization. **Massimo Marro:** Writing – review & editing, Supervision, Methodology, Conceptualization. **Marco Ravina:** Writing – review & editing, Supervision, Conceptualization. **Deborah Panepinto:** Writing – review & editing, Supervision, Funding acquisition, Conceptualization. **Mariachiara Zanetti:** Writing – review & editing, Supervision, Funding acquisition, Conceptualization. **Lionel Souhac:** Writing – review & editing, Supervision, Methodology, Conceptualization. **Pietro Salizzoni:** Writing – review & editing, Supervision, Resources, Project administration, Methodology, Funding acquisition, Conceptualization.

### Declaration of competing interest

The authors declare that they have no known competing financial interests or personal relationships that could have appeared to influence the work reported in this paper.

### Acknowledgments

The authors warmly thank Horacio Correia for his technical support during the wind tunnel experimental campaign, as well as Mariam Manna and Antoine Duclaux, who carefully performed part of the velocity measurements as internship students.

### Appendix A. Mathematical description of model distributions

#### A.1. Gamma distribution

The gamma distribution has a PDF of the form:

$$PDF_{\Gamma}(c) = \frac{c^{k-1} \exp(-c/\theta)}{\Gamma(k)\theta^k}$$

where  $k = \frac{1}{i_C^2}$  and  $\theta = \frac{\bar{C}}{k}$  are the shape and scale parameters, respectively.

The mean, standard deviation, fluctuation intensity, skewness and kurtosis are respectively computed by the following relations:

$$\bar{C} = k\theta$$

$$\sigma_C = \bar{C}/k$$

$$i_C = 1/\sqrt{k}$$

$$Sk = 2/\sqrt{k}$$

$$Ku = (6/k) + 3$$

The percentiles are not given analytically. We compute them from the gamma distribution obtained from the experimental mean and standard deviation of concentration.

#### A.2. 2P-Weibull distribution

The 2-parameter Weibull PDF is given by:

$$PDF_W(c) = \beta\alpha(\beta c)^{\alpha-1} \exp(-(\beta c)^\alpha)$$

where  $\alpha$  is defined from  $i_C^2 = \frac{\Gamma(1+\frac{2}{\alpha})}{[\Gamma(1+\frac{1}{\alpha})]^2} - 1$ , but can be approximated by

$\alpha \simeq (1/i_C)^{1.086}$  and is called the shape parameter. The scale parameter is  $\beta = \Gamma(1 + \frac{1}{\alpha})/\bar{C}$  (Yee et al., 1993b; Oettl and Ferrero, 2017)

Statistical moments (mean, skewness and kurtosis) are computed as:

$$\bar{C} = \frac{1}{\beta} \Gamma(1 + \frac{1}{\alpha})$$

$$Sk = \frac{\Gamma(1 + 3/\alpha) - 3\Gamma(1 + 1/\alpha)\Gamma(1 + 2/\alpha) + 2\Gamma^3(1 + 1/\alpha)}{[\Gamma(1 + 2/\alpha) - \Gamma^2(1 + 1/\alpha)]^{3/2}}$$

$$Ku = \frac{\Gamma(1 + 4/\alpha) - 4\Gamma(1 + 1/\alpha)\Gamma(1 + 3/\alpha) + 6\Gamma^2(1 + 1/\alpha)\Gamma(1 + 2/\alpha) - 3\Gamma^4(1 + 1/\alpha)}{[\Gamma(1 + 2/\alpha) - \Gamma^2(1 + 1/\alpha)]^2}$$

Peak to mean ratios computed from the  $p$  percentile are obtained analytically as:

$$R_p = \frac{[-\log(1-p)]^{1/\alpha}}{\beta \bar{C}}$$

#### A.3. Lognormal distribution

The PDF of the lognormal distribution expands as:

$$PDF_L(c) = \frac{1}{c\lambda\sqrt{2\pi}} \exp\left(-\frac{(\ln(c) - \mu)^2}{2\lambda^2}\right)$$

where  $\lambda = \ln(i_C^2 + 1)^{1/2}$  and  $\mu = \ln(\bar{C}) - \frac{\lambda^2}{2}$  correspond to the standard deviation and average of the logarithm of concentration.

Statistical moments (mean, fluctuation intensity, skewness and kurtosis) are thus (Yee et al., 1993b):

$$\bar{C} = \exp\left(\mu + \frac{\lambda^2}{2}\right)$$

$$i_C^2 = \exp(\lambda^2) - 1$$

$$Sk = \frac{[\exp(\lambda^2)]^3 - 3 \exp(\lambda^2) + 2}{[\exp(\lambda^2) - 1]^{3/2}}$$

$$Ku = \frac{[\exp(\lambda^2)]^6 - 4[\exp(\lambda^2)]^3 + 6 \exp(\lambda^2) - 3}{[\exp(\lambda^2) - 1]^2}$$

Percentiles are not given analytically and are thus computed from the lognormal distribution with parameters  $\lambda$  and  $\mu$  obtained from the experimental data for each point.

## Appendix B. Kullback–Leibler divergence

The Kullback–Leibler divergence (Kullback and Leibler, 1951) is defined as

$$D_{KL}(P \parallel Q) = \sum_{x \in X} P(x) \log(P(x)/Q(x))$$

where  $P(x)$  is the probability of the value  $x$  given by the observed distribution and  $Q(x)$  the probability of  $x$  given by the model distribution.

Lower values of the Kullback–Leibler divergence thus correspond to a better agreement between the model and observed distributions.

## Data availability

Data will be made available on request.

## References

- Andronopoulos, S., Grigoriadis, D., Robins, A., Venetsanos, A., Rafailidis, S., Bartzis, J., 2001. Three-dimensional modelling of concentration fluctuations in complicated geometry. *Environ. Fluid Mech.* 1 (4), 415–440. <http://dx.doi.org/10.1023/A:1015705615846>.
- Ardeshiri, H., Cassiani, M., Park, S.Y., Stohl, A., Pisso, I., Dinger, A.S., 2020. On the convergence and capability of the Large-Eddy Simulation of concentration fluctuations in passive plumes for a neutral boundary layer at infinite Reynolds number. *Bound.-Layer Meteorol.* 176 (3), 291–327. <http://dx.doi.org/10.1007/s10546-020-00537-6>.
- Arnold, S.J., ApSimon, H., Barlow, J., Belcher, S., Bell, M., Boddy, J.W., Britter, R., Cheng, H., Clark, R., Colville, R.N., Dimitroulopoulou, S., Dobre, A., Grealley, B., Kaur, S., Knights, A., Lawton, T., Makepeace, A., Martin, D., Neophytou, M., Neville, S., Nieuwenhuijsen, M., Nickless, G., Price, C., Robins, A., Shallcross, D., Simmonds, P., Smalley, R.J., Tate, J., Tomlin, A.S., Wang, H., Walsh, P., 2004. Introduction to the DAPPLE air pollution project. *Sci. Total Environ.* 332 (1), 139–153. <http://dx.doi.org/10.1016/j.scitotenv.2004.04.020>.
- Bi, D., Mishra, A., Placidi, M., Robins, A., Carpentieri, M., 2025. Wind tunnel study of source location effects on pollutant dispersion around uniform tall building clusters. *J. Wind Eng. Ind. Aerodyn.* 266, 106194. <http://dx.doi.org/10.1016/j.jweia.2025.106194>.
- Carpentieri, M., Hayden, P., Robins, A.G., 2012. Wind tunnel measurements of pollutant turbulent fluxes in urban intersections. *Atmos. Environ.* 46, 669–674. <http://dx.doi.org/10.1016/j.atmosenv.2011.09.083>.
- Cassiani, M., Ardeshiri, H., Pisso, I., Salizzoni, P., Marro, M., Stohl, A., Stebel, K., Park, S.Y., 2024. The dynamics of concentration fluctuations within passive scalar plumes in a turbulent neutral boundary layer. *J. Fluid Mech.* 1001, A18. <http://dx.doi.org/10.1017/jfm.2024.861>.
- Cassiani, M., Bertagni, M.B., Marro, M., Salizzoni, P., 2020. Concentration fluctuations from localized atmospheric releases. *Bound.-Layer Meteorol.* 177 (2), 461–510. <http://dx.doi.org/10.1007/s10546-020-00547-4>.
- Del Ponte, A.V., Fellini, S., Marro, M., van Reeuwijk, M., Ridolfi, L., Salizzoni, P., 2024. Influence of street trees on turbulent fluctuations and transport processes in an urban canyon: A wind tunnel study. *Bound.-Layer Meteorol.* 190 (2), 6. <http://dx.doi.org/10.1007/s10546-023-00843-9>.
- Efthimiou, G.C., Andronopoulos, S., Toliás, I., Venetsanos, A., 2016. Prediction of the upper tail of concentration distributions of a continuous point source release in urban environments. *Environ. Fluid Mech.* 16 (5), 899–921. <http://dx.doi.org/10.1007/s10652-016-9455-2>.
- Fackrell, J.E., 1980. A flame ionisation detector for measuring fluctuating concentration. *J. Phys. E: Sci. Instruments* 13 (8), 888–893. <http://dx.doi.org/10.1088/0022-3735/13/8/021>.
- Fackrell, J.E., Robins, A.G., 1982a. Concentration fluctuations and fluxes in plumes from point sources in a turbulent boundary layer. *J. Fluid Mech.* 117, 1–26. <http://dx.doi.org/10.1017/S0022112082001499>.
- Fackrell, J.E., Robins, A.G., 1982b. The effects of source size on concentration fluctuations in plumes. *Bound.-Layer Meteorol.* 22 (3), 335–350. <http://dx.doi.org/10.1007/BF00120014>.
- Gailis, R.M., Hill, A., 2006. A wind-tunnel simulation of plume dispersion within a large array of obstacles. *Bound.-Layer Meteorol.* 119 (2), 289–338. <http://dx.doi.org/10.1007/s10546-005-9029-1>.
- Gailis, R.M., Hill, A., Yee, E., Hilderman, T., 2007. Extension of a fluctuating plume model of tracer dispersion to a sheared boundary layer and to a large array of obstacles. *Bound.-Layer Meteorol.* 122 (3), 577–607. <http://dx.doi.org/10.1007/s10546-006-9118-9>.
- Hanna, S.R., 1984. The exponential probability density function and concentration fluctuations in smoke plumes. *Bound.-Layer Meteorol.* 29 (4), 361–375. <http://dx.doi.org/10.1007/BF00120535>.
- Hsieh, K.-J., Lien, F.-S., Yee, E., 2007. Numerical modeling of passive scalar dispersion in an urban canopy layer. *J. Wind Eng. Ind. Aerodyn.* 95 (12), 1611–1636. <http://dx.doi.org/10.1016/j.jweia.2007.02.028>.
- Irwin, H.P.A.H., 1981. The design of spires for wind simulation. *J. Wind Eng. Ind. Aerodyn.* 7 (3), 361–366. [http://dx.doi.org/10.1016/0167-6105\(81\)90058-1](http://dx.doi.org/10.1016/0167-6105(81)90058-1).
- Kullback, S., Leibler, R.A., 1951. On information and sufficiency. *Ann. Math. Stat.* 22 (1), 79–86. <http://dx.doi.org/10.1214/aoms/117729694>.
- Lim, H.D., Vanderwel, C., 2023. Turbulent dispersion of a passive scalar in a smooth-wall turbulent boundary layer. *J. Fluid Mech.* 969, A26. <http://dx.doi.org/10.1017/jfm.2023.562>.
- Lung, T., Müller, H.-J., Gläser, M., Möller, B., 2002. Measurements and modelling of full-scale concentration fluctuations. *Agrotechnische Forsch.* 8, 5–15.
- Marucci, D., Carpentieri, M., 2020. Dispersion in an array of buildings in stable and convective atmospheric conditions. *Atmos. Environ.* 222, 117100. <http://dx.doi.org/10.1016/j.atmosenv.2019.117100>.
- Mavroidis, I., Andronopoulos, S., Venetsanos, A., Bartzis, J.G., 2015. Numerical investigation of concentrations and concentration fluctuations around isolated obstacles of different shapes. Comparison with wind tunnel results. *Environ. Fluid Mech.* 15 (5), 999–1034. <http://dx.doi.org/10.1007/s10652-015-9394-3>.
- Melo, A.L.V., Santos, J.M., Reis, N.C., Castro, I.P., V Goulart, E., Xie, Z.T., 2023. Influence of wind direction and source location on peak-to-mean concentration ratios in urban environments. *J. Wind Eng. Ind. Aerodyn.* 232, 105264. <http://dx.doi.org/10.1016/j.jweia.2022.105264>.
- Nironi, C., Salizzoni, P., Marro, M., Mejean, P., Grosjean, N., Soulhac, L., 2015. Dispersion of a passive scalar fluctuating plume in a turbulent boundary layer. Part I: Velocity and concentration measurements. *Bound.-Layer Meteorol.* 156 (3), 415–446. <http://dx.doi.org/10.1007/s10546-015-0040-x>.
- Oettl, D., Ferrero, E., 2017. A simple model to assess odour hours for regulatory purposes. *Atmos. Environ.* 155, 162–173. <http://dx.doi.org/10.1016/j.atmosenv.2017.02.022>.
- Ono, A., Nozu, T., 2024. Comparison between wind tunnel experiment and Large-Eddy Simulation of concentration fluctuations in pollutant dispersion in a realistic urban area. *J. Wind Eng. Ind. Aerodyn.* 253, 105832. <http://dx.doi.org/10.1016/j.jweia.2024.105832>.
- Papp, B., Istók, B., Koren, M., Balczó, M., Kristóf, G., 2024. Statistical assessment of the concentration fluctuations in street canyons via time-resolved wind tunnel experiments. *J. Wind Eng. Ind. Aerodyn.* 246, 105665. <http://dx.doi.org/10.1016/j.jweia.2024.105665>.
- Pearce, W., Baker, C.J., 1999. Wind tunnel tests on the dispersion of vehicular pollutants in an urban area. *J. Wind Eng. Ind. Aerodyn.* 80 (3), 327–349. [http://dx.doi.org/10.1016/S0167-6105\(98\)00114-7](http://dx.doi.org/10.1016/S0167-6105(98)00114-7).
- Salizzoni, P., Fellini, S., Gamel, H., Marro, M., Soulhac, L., 2025. Atmospheric dispersion downstream a two-dimensional obstacle: Experimental evaluation of turbulence closure models. *Bound.-Layer Meteorol.* 191 (3), 15. <http://dx.doi.org/10.1007/s10546-025-00905-0>.
- Talluru, K.M., Hernandez-Silva, C., Philip, J., Chauhan, K.A., 2017. Measurements of scalar released from point sources in a turbulent boundary layer. *Meas. Sci. Technol.* 28 (5), 055801. <http://dx.doi.org/10.1088/1361-6501/aa614a>.
- Xie, Z.-T., Hayden, P., Robins, A.G., Voke, P.R., 2007. Modelling extreme concentrations from a source in a turbulent flow over a rough wall. *Atmos. Environ.* 41 (16), 3395–3406. <http://dx.doi.org/10.1016/j.atmosenv.2006.12.022>.
- Yee, E., Biltoft, C.A., 2004. Concentration fluctuation measurements in a plume dispersing through a regular array of obstacles. *Bound.-Layer Meteorol.* 111 (3), 363–415. <http://dx.doi.org/10.1023/B:BOUN.0000016496.83909.ee>.
- Yee, E., Chan, R., Kosteniuk, P.R., Chandler, G.M., Biltoft, C.A., Bowers, J.F., 1994. Experimental measurements of concentration fluctuations and scales in a dispersing plume in the atmospheric surface layer obtained using a very fast response concentration detector. *J. Appl. Meteorol. Clim.* 33 (8), 996–1016. [http://dx.doi.org/10.1175/1520-0450\(1994\)033<0996:EMOCFA>2.0.CO;2](http://dx.doi.org/10.1175/1520-0450(1994)033<0996:EMOCFA>2.0.CO;2).
- Yee, E., Kosteniuk, P.R., Chandler, G.M., Biltoft, C.A., Bowers, J.F., 1993a. Statistical characteristics of concentration fluctuations in dispersing plumes in the atmospheric surface layer. *Bound.-Layer Meteorol.* 65 (1), 69–109. <http://dx.doi.org/10.1007/BF00708819>.
- Yee, E., Wilson, D.J., Zelt, B.W., 1993b. Probability distributions of concentration fluctuations of a weakly diffusive passive plume in a turbulent boundary layer. *Bound.-Layer Meteorol.* 64 (4), 321–354. <http://dx.doi.org/10.1007/BF00711704>.